13th International Symposium on Particle Image Velocimetry – ISPIV 2019
Munich, Germany, July 22-24, 2019

Force estimates in turbulent vortex wakes of accelerating propulsors: The effects of edge undulation on vortex formation

Frieder Kaiser[1,2*], Joshua Galler[1], Jochen Kriegseis[2], David E. Rival[1]

[1] Department of Mechanical and Materials Engineering, Queen's University, Kingston, Ontario, Canada

[2] Institute of Fluid Mechanics, Karlsruhe Institute of Technology (KIT), Karlsruhe, Germany

[*] frieder.kaiser@kit.edu

Abstract

The effects of edge undulation on separated flows and vortex formation are investigated with various geometries of accelerated, low aspect-ratio propulsors. In addition to force measurements, multi-camera planar particle image velocimetry (PIV) is applied for a large field of view of approximately $1.9\,\mathrm{m} \times 0.3\,\mathrm{m}$. Edge undulations with a wavelength λ, that is significantly larger than the thickness δ of the separated shear layer are identified to enhance the propulsion force during the stable vortex growth and before the vortex detaches. Edge undulation leads to a more turbulent vortex core and a faster vortex growth. The application of different approaches to recover the acting forces from PIV data lead to the conclusion, that the three-dimensionality of the turbulent vortex wake leads to both: a loss of out-of-plane vorticity and an underestimation of the kinetic energy in the vortex.

1 Introduction

Enhancing turbulence by means of passive flow control is well established in quasi-steady aerodynamics. Examples include leading-edge modifications on airfoils (Lissaman, 1983) and noise reduction in the wake of turbo-fan engines by lobed mixers (Knowles and Saddington, 2006). In contrast, little is known on the influence of such modifications on the roll-up of separated shear layers in the vortex wake of accelerated propulsors. A change of the angle of attack of the fluid relative to the propulsor leads to flow separation at the vortex forming edge (VFE), which is marked blue in figure 1(a). While a large variety of swimmers and flyers form leading-edge vortices (LEV) and trailing-edge vortices (TEV) for efficient propulsion, not all propulsors display smooth and straight edges. Among others, the propulsors of frogs (Johansson and Lauder, 2004), sea-lions (Sawyer et al., 2016) and humpback whales (Fish et al., 2011) posses undulatory leading/trailing edges; see figure 1(a). Kaiser et al. (2019) assess the influence of various VFE modifications on impulsively accelerated low-aspect ratio propulsor for a large range of Reynolds numbers (*Re*) by means of force measurements and particle image velocimetry (PIV). By analyzing the measured differences in propulsion force and, the ratio

$$B = \lambda / 2\delta \tag{1}$$

of undulation wavelength λ (see figure 1(a)) and the shear-layer thickness δ is identified as the critical quantity if the undulations influence the vortex formation. The present study strives to extend the observations of Kaiser et al. (2019) by estimating the measured forces from PIV data. In particular, the influence of turbulence on the circulation budget and the different force-estimation techniques are applied.

2 Methods and procedure

Based on the findings of Fernando and Rival (2016) the reference case of this study is selected: a circular plate of diameter D; figure 1(b). The plate is accelerated from rest perpendicular to its orientation. The forming vortex remains relatively stable for many diameters traveled ($s^* = s/D$, where s is the traveled distance)

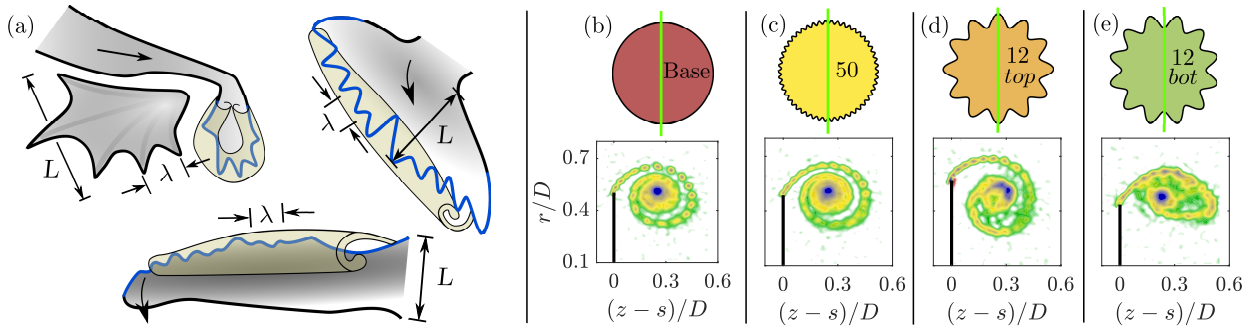

Figure 1: (a) Examples of undulatory VFE modifications in nature (frog, humpback whale, and sea lion). (b)-(e) different geometries and measurement planes (light green lines) and the respective vorticity fields at a $s^* = 1.25$ ($Re = 350000$)

and thus allows a detailed investigation of the vortex before it eventually detaches. After a short acceleration over the distance $s^* = s/D = 0.5$, the plate travels with a constant terminal velocity U_∞. Experiments for two different final velocities U_∞ and thus $Re = U_\infty D/\nu$ were conducted ($Re = 50000$ & $Re = 350000$, ν is the kinematic viscosity). To assess the impact of VFE modifications four different plates with undulations of

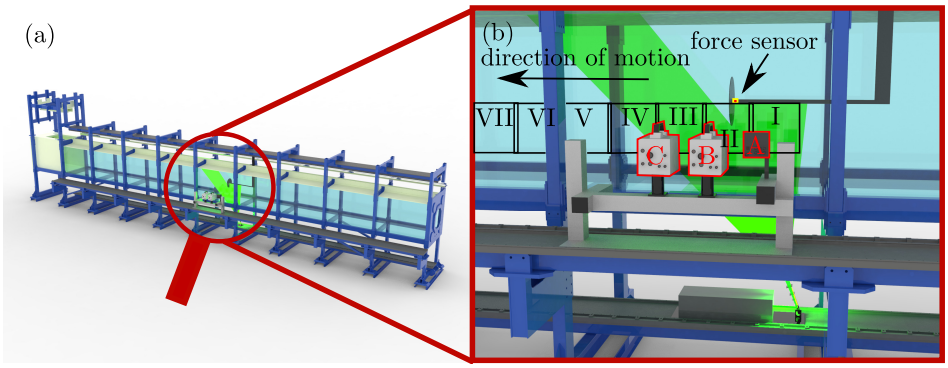

Figure 2: (a) Towing tank facility at Queen's University; (b) Experimental setup with cameras A-C, FOV I-VII, the setup of the plate, the force sensor, and the location of the laser sheet.

varying wavelengths λ were tested (Kaiser et al., 2019). n_p undulations of length $\lambda = \pi D/n_p$ are imprinted along the plates circumference. Wavelength λ and amplitude a of the undulations are held at a constant ratio of $a/\lambda = 1/4$. The radius of the modified plates is given by

$$r(\varphi) = D/2 + \lambda/4\cos(n_p\varphi). \tag{2}$$

Note that for all geometries the frontal area $A = \int_{\tilde{r}=0}^{r(\varphi)} \int_{\varphi=0}^{2\pi} \tilde{r}^2 \mathrm{d}\varphi\mathrm{d}\tilde{r}$ is kept constant. Figure 1(b)-(e) presents three of the four investigated geometries with $n_p \in \{\infty, 200, 50, 12\}$. The wavelengths are chosen in such a way, that $n_p = 50$ coincides with a undulation height $2a$, that is similar to the shear-layer thickness δ at the VFE. Therefore, $n_p = 12$ and $n_p = 200$ introduce disturbances in wavelenghts larger and smaller than δ, respectively.

The effects of the various plates on vortex formation were tested in a 15 m-long optical towing tank with a 1×1 m cross section (see figure 2(a)). Optically accessible from three sides, the water-filled test section is semi-enclosed on the top to minimize free surface effects. The various plate geometries were connected to the traverse mounted above the tank via a cylindrical sting of diameter $0.08D$ and length $2D$ and a symmetric profile of thickness $0.08D$ (see figure 2(b)).

The force acting from the fluid on the propulsor and *vice versa* (propulsion force) was directly measured with a six-component, submersible ATI Nano force transducer, mounted between the sting and the plate as presented in figure 2(b). The force data were collected with a static resolution of 0.125 N at a rate of 1000 Hz

for $0 < s^* < 33$. All geometries were tested at both terminal velocities U_∞. Each parameter combination was repeated 20 times and the results were ensemble-averaged to reduce noise.

In addition to the force measurements, the flow fields around the plates were captured by means of time-resolved planar PIV. A 40 mJ/pulse Photonics high-speed laser produced a light sheet of 2 mm thickness. The light sheet was introduced from below the tank and aligned parallel to the side walls. Tilting the light-sheet slightly towards the direction of the acceleration avoided shadows in the wake of the plate. Three cameras, mounted in a lab-fixed frame of reference captured the flow evolution for $0 < s^* < 6.1$ in three consecutive measurement campaigns. During the first measurement campaign, the field of view (FOV) $s^* = 0-2.3$ was covered by all three cameras (A,B,C, see figure 2(b)). The acceleration $s^* < 0.5$ is captured in a $0.7D \times 0.7D$ FOV (I) with a Photron Fastcam Mini WX100 (2048×2048, camera A) to ensure a high spatial resolution near the VFE. Two additional Photron SA4 cameras (1024×1024 pixels, cameras B & C) cover the further evolution of the vortex each recording an area of $0.85D \times 0.85D$ (II & III). Utilizing AF-S Micro-Nikkor 60mm 1:2.8G ED lenses on all cameras resolutions of 9.8 px/mm (FOV I) and 4 px/mm (FOVs II & III) could be achieved. Cameras B & C were further used to capture the later stages of vortex evolution in FOV IV & V (campaign 2) and VI & VII (campaign 3). To account for vortex growth, the FOV was increased to $1.0D \times 1.0D$, which resulted in a spatial resolution of 3.4 px/mm. The PIV measurements were repeated 20 times for each plate geometry-*Re* combination during all three campaigns. For the $n_p = 12$ plate, all measurements were performed twice. The light sheet was first aligned with the maximum of the plate radius (see figure 1(d)). Subsequently, the experiments were repeated and the plate was rotated to align the laser sheet with the minimum of the plate radius (see figure 1(e)). The experiments are referred to as $12top$ and $12bot$ in the following.

Ensemble-based median subtraction, plate tracking and masking of the shadowed area was performed in MATLAB. Consecutively, the data were calibrated and processed in DaVis 8.4 with a multi-grid scheme (final interrogation area 32×32 pixels, 75% overlap). The resulting data of all runs were eventually merged into a single plate-fixed grid. Due to accurate calibration, plate tracking and good reproducibility of the flow, the data of the different campaigns could be stitched into a single FOV of approximately 1.9 m $\times$0.3 m. In a final step, the data is ensemble averaged, to reduce noise.

3 Results

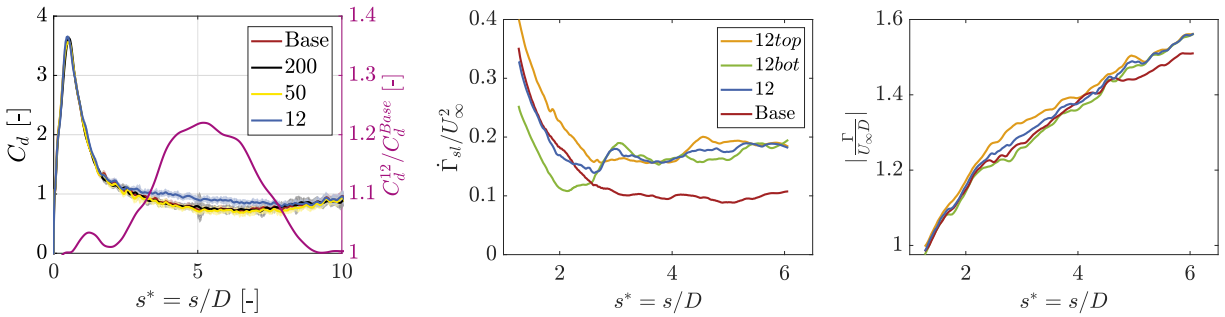

Figure 3: (a) Directly measured forces of the different propulsors for $Re = 350000$, ratio C_d^{12}/C_d^{Base} of the drag coefficient of the $n_p = 12$ plate and the circular reference case; (b) Circulation flux $\dot{\Gamma}_{sl}$ into the vortex by the shear-layer, blue line represents the average of $12top$ and $12bot$; (c) overall circulation Γ in the vortex core.

Figure 3(a) presents the measured forces for $Re = 350k$ and all plate geometries. The data were ensemble-averaged over 20 runs and temporally filtered with a least-square estimator; see Savitzky and Golay (1964). The propulsion forces F_z were further normalized, leading to the drag coefficient

$$C_d = \frac{2F_z}{\rho A U_\infty^2}, \tag{3}$$

where ρ is the density of water. Two standard deviations of the run-to-run scatter 2σ are added to the plot. During the acceleration stage $s^* \leq 0.5$ and the relaxation stage $s^* < 2$, the forces of all geometries

collapse. However, during the stage of stable vortex growth and before the vortex eventually detaches from the plate ($s^* < 9$), the $n_p = 12$ plate allows to exert up to 20% higher forces than the reference case of a smooth circular plate. Note that the ratio C_d^{12}/C_d^{Base} was added to the diagram (magenta line, right ordinate in figure 3(a)) to emphasize this difference. In case λ is not significantly larger than δ ($B \leq 1$, plates with $n_p = 50$ and $n_p = 200$), no measurable effect of the undulations on the forces was detected. Thus the following discussion is limited to the long wavelength plate ($n_p = 12$) and its comparison to the circular base case. First, the vortex circulation is analyzed. Pitt Ford and Babinsky (2013) motivate the importance

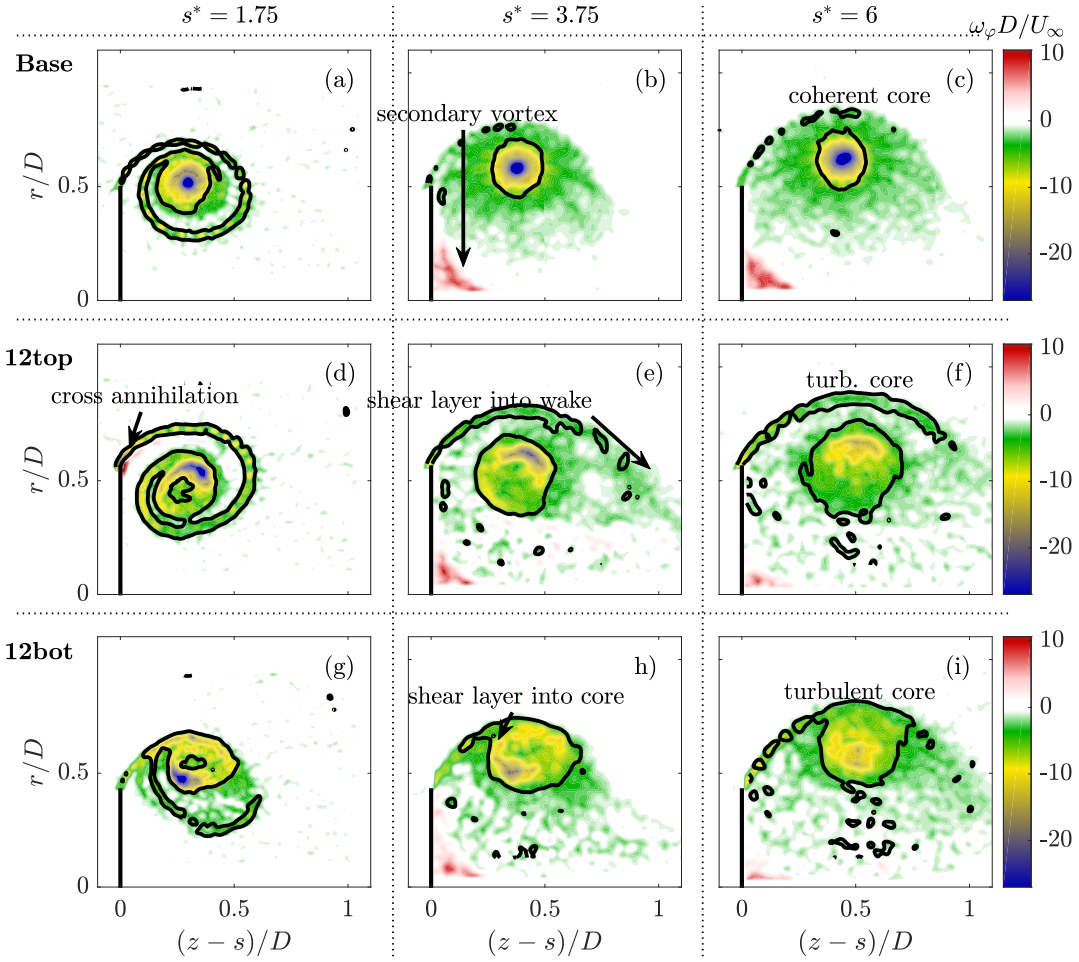

Figure 4: Vortex formation for the circular plates and $n_p = 12$ at $Re = 350$k: Stronger shear layer, higher turbulence level and more diffuse vortex core for the $n_p = 12$ plate. Secondary vortex near the plate center for both cases. Black solid lines: vortex boundaries of $\Gamma_2 = 2/\pi$.

of circulation on the forces induced by an unsteady vortex. Most circulation bound to the propulsor is found in the separated vortical structure. As such, the vortex circulation strongly correlates to the exerted force. Figure 4 shows the determined vorticity fields ω_φ for *Base*, 12*top* and 12*bot* and three different time instances. The circulation of the vortex is fed by the shear-layer. A more pronounced shear layer for the undulated plate (figure 4(e,f,g,h)) suggests a faster circulation growth. Therefore, the feeding rate

$$\dot{\Gamma}_{sl}(t) = \int_\delta u_{sl}\omega_\varphi \mathrm{d}n \tag{4}$$

is estimated by integrating the vorticity flux over the shear-layer thickness. u_{sl} is the velocity tangential to the shear-layer and n is the direction normal to the shear layer. Indeed, figure 3(b) presents a larger $\dot{\Gamma}_{sl}(t)$

for the undulated plate. However, the overall circulation $\Gamma(t)$ in the vortex

$$\Gamma(t) = \int_{FOV} \omega_\varphi \mathrm{d}A, \tag{5}$$

as presented in figure 3(c), shows similar slopes for both geometries. The similar evolution of $\Gamma(t)$ despite varying feeding rates $\dot{\Gamma}_{sl}(t)$ can be explained by multiple effects apparent in figure 4. First, the vortex wake of the undulated plate is more turbulent. While the vortex core of the circular plate is coherent and contains high values of ω_φ, the core of plate 12 is more diffuse and of larger spacial extent. The vortex core area is highlighted by the Γ_2-criterion formulated by Graftieaux et al. (2001). A more turbulent core results in reorientation of vorticity and a reduction of ω_φ. Second, cross-annihilation of vorticity with opposite signed vorticity convecting from the plate (see figure 4(d)) also reduces the circulation of plate 12. In addition, the interaction of the turbulent vortex core with the secondary vortex near the center of the plate is more pronounced for the undulated plate. The accumulation of the circulation reducing effects compensates for the differences in the feeding shear-layer and as a result, the evolution of circulation remains similar. In combination with the similar vortex radius for both geometries (see figure 5(a), radius based on the maximum of the Q-criterion as introduced by Hunt et al. (1988)) the similar evolution of the circulation leads to the conclusion, that simple vortex force models as suggested by Lamb (1932) cannot explain the force difference between the circular and the undulated plate. Lamb (1932) showed that the force produced by a counter-rotating vortex pair can be described as

$$F = \Gamma U_\infty + \frac{\partial \Gamma}{\partial t} 2 r_c, \tag{6}$$

where $2r_c$ is the distance between the vortices. Another simple approach to estimate the vortex forces is based on the vortex size. The higher level of turbulence in the wake of plate 12 suggests a higher entrainment rate and as such a faster vortex growth. The axial vortex position presented in dashed lines in figure 5(a) supports this idea, as it shows a more distant vortex for the undulated plate. Neglecting the momentum in the vortex rotation, the impulse of the moving plate with its attached vortex is modeled as a solid body with size $V(t)$ that can be described by

$$I_m = [\rho V(t) + m_p(t)] U_\infty(t). \tag{7}$$

Hereby, the coefficient $m_p(t)$ describes the vorticity free area around the vortex. For $s^* > 0.5$ the plate velocity U_∞ is constant. Thus, the force is estimated as

$$F_m = \dot{I_m} = [\rho \dot{V}(t) + \dot{m_p}(t)] U_\infty. \tag{8}$$

The vortex volume $V(t)$ is determined by topology analysis. The streamline leading to the node behind the plate is identified as exemplarily highlighted in figure 5(b). The axisymmetric volume under the streamline is defined as $V(t)$. In case of the undulated plate, the volume is approximated by linear interpolation between $12bot$ and $12top$ (blue line in figure 5(c)). As expected a faster vortex growth is observed. The contribution of the vortex volume growth $C_d^V = 2\dot{V}(t)/AU_\infty$ to the overall drag coefficient C_d during the later stages of the PIV data ($2.5 < s^* < 6$) accounts in large parts for the measured increased drag of plate 12 ($C_d^V(Base) = 0.4$ and $C_d^V(12) = 0.48$). A more elaborate approach to account for the impulse changes of the fluid and its relation to the fluid-structure interaction is taken by Galler et al. (2019). Extending the principle of added-mass (see e.g. Brennen (1982)) to a separated flow, the virtually accelerated mass is not gained by means of a potential flow solution, but estimated by means of the measured PIV data. This mass coefficient m_E, in the following referred to as the *energized mass* is defined as

$$m_E = \frac{\rho \int_V u^2 \mathrm{d}V}{U_\infty^2}, \tag{9}$$

where $u(r, \varphi, z, t)$ is the velocity magnitude in the flow. In a cylindrical coordinate system and assuming axisymmetry m_E can be approximated with the PIV data by

$$m_E = \frac{2\pi\rho \int_{z_{min}}^{z_{max}} \int_{r=0}^{r_{max}} u^2 r \mathrm{d}r \mathrm{d}z}{u_b^2} = \frac{2\pi\rho A_e \sum_r \sum_z u^2 r}{u_b^2}, \tag{10}$$

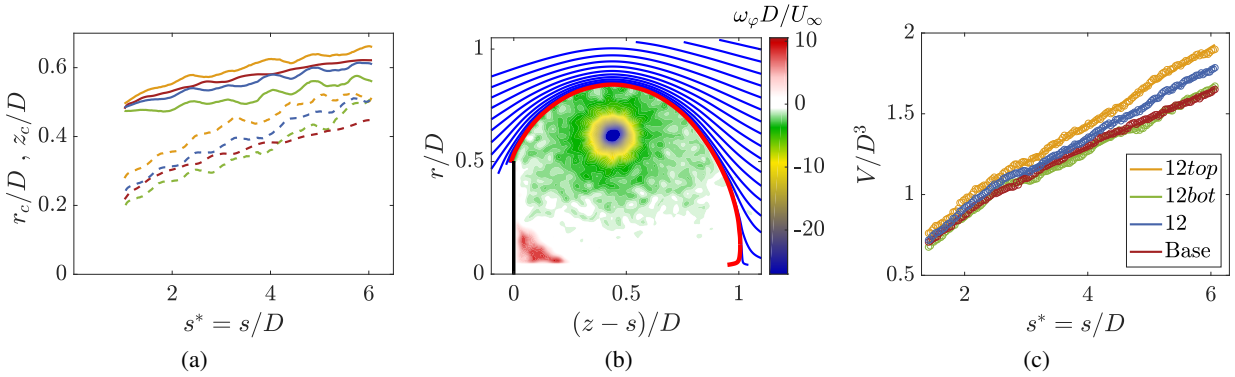

Figure 5: (a) Vortex center identified by the maximum of the Q-criterion, solid lines: radial position r_c, dashed lines: axial position z_c; (b) vortex size estimation based on flow topology, streamline in red depicts the vortex boundary; (c) vortex volume for the $n_p = 12$ plate and the circular base case.

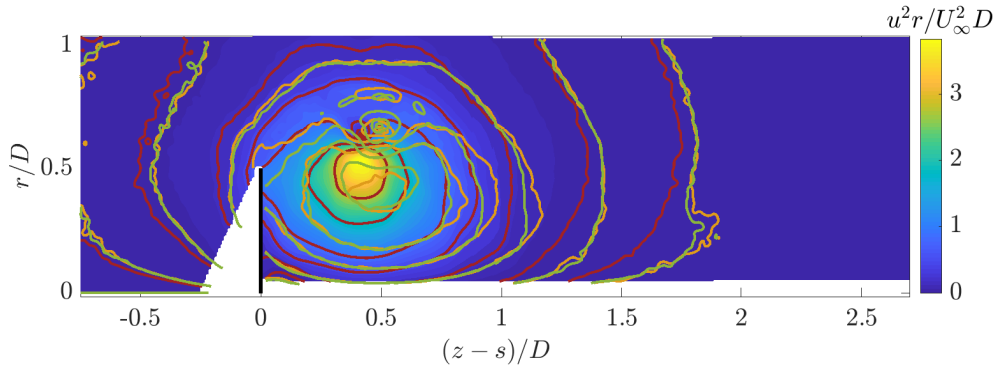

Figure 6: $u^2 r$ at $s^* = 5$. Filled contour presents the data of the circular plate, contour lines depict equivalent levels for the circular base case (red), $12top$ (orange) and $12bot$ (green).

A_e is the physical size of an interrogation area. Note that evaluation of equation 10 in the given FOV only approximates m_E, as the area of accelerated fluid extends over the boundaries of the FOV and the area in front of the plate could not be measured due to the plate's shadow. Figure 6 shows $u^2 r$ for the $12bot$, $12top$ and the circular plate. The larger vortex size of the undulated plate is captured by the outer isocontours. However, the coherent vortex core of the circular plate contains significantly more kinetic energy than the turbulent core of the undulated plate. As such, the evolution of m_E^{mean}, which is the energized mass based on the ensemble averaged data grows faster for the circular plate; see figure 7(a). The evaluation of m_E for the single runs of the PIV measurements are shown as grey dots in figure 7(a). The significantly larger run-to-run scatter for the undulated plate again emphasizes the existence of turbulence in the wake of plate 12. The additional energized mass due to the kinetic energy of the fluctuations m_E^{fluct} in the measurement plane is presented in figure 7(b). Estimating the forces by means of the impulse change for the accumulated energized mass $m_E = m_E^{mean} + m_E^{fluct}$ leads to

$$F_{EM} = \frac{\mathrm{d}(m_E U_\infty)}{\mathrm{d}t}. \tag{11}$$

and the drag coefficients $C_d = 2F_{EM}/\rho A U_\infty^2$. Figure 7(c) presents the temporal evolution of the estimated C_d (solid lines) in comparison to the data measured by the force sensor (dashed lines). While the quasi-two-dimensional flow in the wake of the circular plate allows accurate estimations of m_E and therefore of the force, the energized mass of the $n_p = 12$ plate is underestimated. Non-negligible out of plane velocities in the wake of the undulated force are not captured by the planar measurements and as such the energized mass

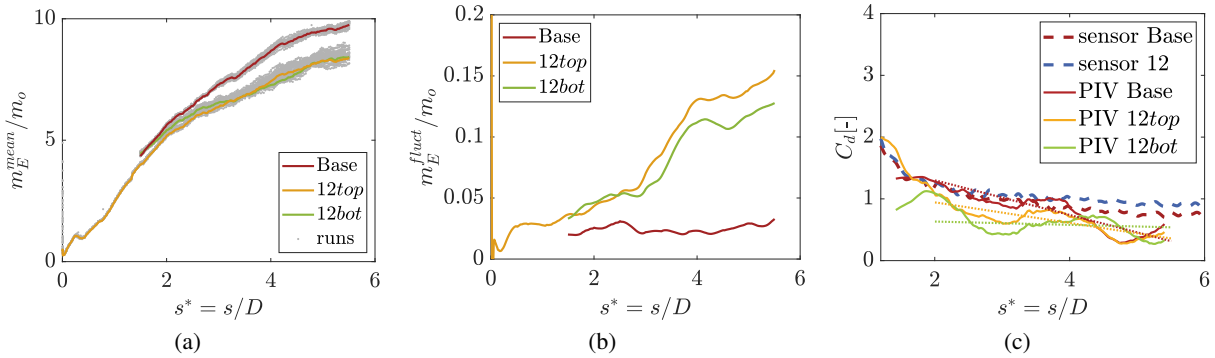

Figure 7: (a) Energized mass m_E^{mean} of the ensemble-averaged data (lines) and the single runs (grey dots); (b) Energized mass m_E^{fluct} of the in-plane fluctuations (c) estimated drag coefficients with the principle of energized mass (solid lines) compared to the measured forces (dashed lines).

is underestimated; cp. figure 7(c).

4 Conclusions

Multiple geometries of accelerated propulsors were tested to investigate the effects of edge undulation on vortex formation. While the effects are small if the wavelength of the undulations λ is similar to the shear-layer thickness δ, larger values of λ lead to an enhanced propulsion force during the vortex growth stage. The present study compares such a large wavelength plate ($n_p = 12$) to a smooth circular reference case. In particular, unsteady planar PIV measurements for a large multi-camera FOV are evaluated to understand the physical mechanisms behind the enhanced forces. The turbulence introduced by the edge undulations leads to modifications of the flow topology. A more pronounced shear-layer feeds the vortex behind the undulated plate. However, the effects of the shear layer are compensated by vorticity annihilating mechanisms in the turbulent vortex core. This yields similar temporal circulation evolutions for undulated and the circular plate. The enhanced propulsion forces of the undulated plate can be in parts explained by a simple model that only accounts for the vortex size to estimate the forces. A more elaborate approach suggested by Galler et al. (2019) (energized mass) was also tested. While the principle of energized mass is able to reconstruct the force evolution for the circular plate, the highly three-dimensional flow behind the undulated geometry led to an underestimation of the forces.

Acknowledgements

The authors greatly acknowledge the support by the Karlsruhe House of Young Scientists (KHYS) for FK's scholarship to support his research abroad in Canada. DER and JG would also like to acknowledge NSERC.

References

Brennen CE (1982) A review of added mass and fluid inertial forces.. Technical report. Naval Engineering Laboratory, Port Hueneme, CA, CR 82.010.

Fernando JN and Rival DE (2016) On vortex evolution in the wake of axisymmetric and non-axisymmetric low-aspect-ratio accelerating plates. *Physics of Fluids* 28

Fish F, Weber P, Murray M, and Howle L (2011) The tubercles on humpback whales' flippers: application of bio-inspired technology. *Integrative and Comparative Biology* 51:203–213

Galler J, Weymouth GD, and Rival DE (2019) Progress towards modelling unsteady forces using a drift-volume approach. *AIAA SciTech Forum 2019* Paper no. 2019-1147

Graftieaux L, Michard M, and Grosjean N (2001) Combining PIV, POD and vortex identification algorithms for the study of unsteady turbulent swirling flows. *Measurement Science and Technology* 12:1422

Hunt JCR, Wray AA, and Moin P (1988) Eddies, streams, and convergence zones in turbulent flows. *Center for Turbulence Research Report CTR-S88* pages 193–208

Johansson LC and Lauder GV (2004) Hydrodynamics of surface swimming in leopard frogs (rana pipiens). *Journal of Experimental Biology* 207:3945–3958

Kaiser F, Kriegseis J, and Rival DE (2019) The inuence of edge undulation on vortex formation for low-aspect-ratio propulsors. *Journal of Fluid Mechanics (under review)*

Knowles K and Saddington A (2006) A review of jet mixing enhancement for aircraft propulsion applications. *Proceedings of the Institution of Mechanical Engineers, Part G: Journal of Aerospace Engineering* 220:103–127

Lamb S (1932) Hydrodynamics. *Cambridge University Press, Cambridge, UK*

Lissaman P (1983) Low-reynolds-number airfoils. *Annual Reviews of Fluid Mechanics* 15:223–239

Pitt Ford CP and Babinsky H (2013) Lift and the leading-edge vortex. *Journal of Fluid Mechanics* 720:280–313

Savitzky A and Golay MJE (1964) Smoothing and differentiation of data by simplified least squares procedures. *Analytical Chemistry* 36:1627–1639

Sawyer EK, Turner EC, and Kaas JH (2016) Somatosensory brainstem, thalamus, and cortex of the california sea lion (zalophus californianus). *Journal of Comparative Neurology* 524:1957–1975